Energy & Environmental Science

ROYAL SOCIETY OF CHEMISTRY

PAPER

View Article Online
View Journal | View Issue

Cite this: *Energy Environ. Sci.*, 2020, **13**, 3032

Atomically dispersed Fe–N–C decorated with Pt-alloy core–shell nanoparticles for improved activity and durability towards oxygen reduction†

Xiang Ao,[ab] Wei Zhang,[c] Bote Zhao,*[a] Yong Ding,[a] Gyutae Nam,[a] Luke Soule,[a] Ali Abdelhafiz,[a] Chundong Wang*[b] and Meilin Liu*[a]

One of the key challenges that hinders broad commercialization of proton exchange membrane fuel cells is the high cost and inadequate performance of the catalysts for the oxygen reduction reaction (ORR). Here we report a composite ORR catalyst consisting of ordered intermetallic Pt-alloy nanoparticles attached to an N-doped carbon substrate with atomically dispersed Fe–N–C sites, demonstrating substantially enhanced catalytic activity and durability, achieving a half-wave potential of 0.923 V (*vs.* RHE) and negligible activity loss after 5000 cycles of an accelerated durability test. The composite catalyst is prepared by deposition of Pt nanoparticles on an N-doped carbon substrate with atomically dispersed Fe–N–C sites derived from a metal–organic framework and subsequent thermal treatment. The latter results in the formation of core–shell structured Pt-alloy nanoparticles with ordered intermetallic Pt_3M (M = Fe and Zn) as the core and Pt atoms on the shell surface, which is beneficial to both the ORR activity and stability. The presence of Fe in the porous Fe–N–C substrate not only provides more active sites for the ORR but also effectively enhances the durability of the composite catalyst. The observed enhancement in performance is attributed mainly to the unique structure of the composite catalyst, as confirmed by experimental measurements and computational analyses. Furthermore, a fuel cell constructed using the as-developed ORR catalyst demonstrates a peak power density of 1.31 W cm^{-2}. The strategy developed in this work is applicable to the development of composite catalysts for other electrocatalytic reactions.

Received 15th March 2020,
Accepted 16th July 2020

DOI: 10.1039/d0ee00832j

rsc.li/ees

Broader context

Proton exchange membrane fuel cells (PEMFCs) are a promising technology to satisfy societal interest in green and efficient energy conversion and storage devices. In order to fully commercialize the technology, cheaper, more efficient, and stable catalysts for the oxygen reduction reaction (ORR) need to be developed and implemented. A new, inexpensive class of materials, single-atom catalysts (SACs), show comparable performance to platinum group metal (PGM) catalysts in alkaline media, while PEMFCs require suitable performance in acidic media because of the successful commercialization of Nafion proton exchange membranes. To overcome this issue, the current work combines SACs with Pt-alloy catalysts to achieve improved performance in acidic media with increased stability and at a lower cost than pure Pt-based materials. The new composite catalyst is comprised of atomically dispersed transition metal sites embedded in a porous carbon substrate that are also alloyed with Pt nanoparticles, which increases the Pt activity and stability against dissolution. In addition, single-atom sites that do not alloy with Pt are also catalytically active and even interact with the Pt alloy, further increasing the overall activity. This work represents a new strategy to develop efficient, stable, and cost-effective catalysts for PEMFCs.

Introduction

Proton exchange membrane fuel cells (PEMFCs) are widely considered one of the promising power sources for automobiles and portable devices due to their high energy efficiency, high power density, and environmental sustainability.[1,2] However, the overall efficiency of PEMFCs is severely hindered by the sluggish kinetics of the oxygen reduction reaction (ORR) on the cathode.[3,4] A catalyst comprised of platinum nanoparticles

[a] *School of Materials Science and Engineering, Georgia Institute of Technology, Atlanta, Georgia 30332, USA. E-mail: bote.zhao@mse.gatech.edu, meilin.liu@mse.gatech.edu*
[b] *Wuhan National Laboratory for Optoelectronics, School of Optical and Electronic Information, Huazhong University of Science and Technology, Wuhan 430074, China. E-mail: apcdwang@hust.edu.cn*
[c] *Beijing Advanced Innovation Center for Soft Matter Science and Engineering, Beijing University of Chemical Technology, Beijing 100029, China*

† Electronic supplementary information (ESI) available: Experimental and computational details, supplementary figures, supplementary tables, and supplementary references. See DOI: 10.1039/d0ee00832j

dispersed on a carbon black support (Pt/C) is typically used to catalyze the ORR, but the high cost and natural scarcity of Pt is an impediment that precludes the wide-spread adoption of PEMFCs. Moreover, Pt catalysts often suffer from activity degradation caused by crystallite dissolution and agglomeration during operation.[5] To overcome these issues, it is desirable to reduce the Pt loading while maintaining its activity and improving the stability, or ultimately to replace Pt group metal (PGM) catalysts with PGM-free catalysts.

To date, catalysts comprised of nitrogen-coordinated iron atoms on a carbon support (Fe–N–C) have been studied as a promising alternative to Pt catalysts due to their encouraging ORR catalytic activity.[6,7] Despite the great progress in their performance in alkaline solution, it is still a huge challenge to achieve high performance for Fe–N–C catalysts in acidic media. However, the development of high-performance ORR catalysts in acidic media is more important for the application of PEMFCs, because of the successful commercialization of Nafion proton exchange membranes. In light of this fact, Pt-based ORR catalysts with improved utilization efficiency and durability may offer more immediate opportunities to commercialize PEMFCs.[8,9]

Enormous efforts have been devoted to optimizing Pt-based catalysts during the past decades. Among them, alloying Pt with a second transition metal and tuning its morphology is an effective strategy.[10–12] It has been demonstrated that structurally ordered intermetallic Pt-alloy nanoparticles showed an improvement in ORR catalytic activity and stability.[10,13,14] Specifically, it has been reported that encasing the ordered intermetallic Pt-alloy core in a Pt-rich shell can achieve further enhanced Pt mass activity for the ORR.[15] Despite the great progress, further improvement of the performance is still desired but challenging. Apart from alloying and structure control, support materials also play a significant role in improving the activity and have attracted much attention.[16] Carbon materials such as carbon black and graphene are extensively used as supports of Pt catalysts due to their excellent electronic conductivity, chemical stability and high surface area.[17,18] However, conventional carbon supports (with a typical weight percentage of 40–60 wt%) are electrocatalytically inactive. Alternatively, transition metal/nitrogen-doped carbon structures such as Fe–N–C are highly electrocatalytically active for the ORR,[7,19] and could offer more active sites compared to conventional carbon supports. Moreover, it has been found that the close proximity between Pt-based alloy nanoparticles and $Co–N_4$ active sites could promote synergistic catalysis.[20] However, the preparation method involves an acid etching process and heat-treatment under toxic ammonia,[20] which is somewhat uneconomical and less environmentally friendly. Accordingly, incorporating Pt-alloy nanoparticles onto an Fe–N–C substrate has potential to significantly enhance the ORR activity. This would be a very attractive strategy for the development of highly active ORR catalysts in acidic media if an environmentally friendly process could be developed for preparation of composite catalysts with desired nanostructure and catalytic mechanism.

In this work, we report our findings on a highly efficient and robust ORR catalyst in acidic media comprised of core–shell ordered intermetallic Pt-alloy nanoparticles embedded onto a porous atomically dispersed Fe–N–C support (denoted as $Pt_A@Fe_{SA}$–N–C, where Pt_A and Fe_{SA} represent the Pt alloy and single atom Fe, respectively), which was prepared by alloying Pt with atomically dispersed atoms in the substrate. The catalyst has multiple active sites for enhancing the catalytic activity and a porous structure for facilitating mass transfer, which enables the as-prepared $Pt_A@Fe_{SA}$–N–C to exhibit outstanding ORR activity with a half-wave potential ($E_{1/2}$) of 0.923 V (*versus* reversible hydrogen electrode (RHE), all potentials obtained using a rotating disk electrode in this work were calibrated with respect to RHE), together with an excellent durability of 7 mV decay in $E_{1/2}$ after a 5000-cycle accelerated durability test (ADT) in an acidic electrolyte. In addition, the Pt loading of the $Pt_A@Fe_{SA}$–N–C catalyst is below that of Pt/C, but its ORR activity is higher than that of Pt/C, making it a promising candidate for next-generation cathode active materials for PEMFCs. Experiments and density functional theory (DFT) calculations demonstrate that the notable ORR performance is ascribed to both the atomically dispersed Fe sites and Pt-alloy nanoparticles and the interaction between them.

Results and discussion

The synthesis procedure of $Pt_A@Fe_{SA}$–N–C is schematically illustrated in Fig. 1a. Briefly, Zn-based zeolitic imidazolate frameworks (ZIF-8) are used as a host to encapsulate Fe ions through an adsorption approach in a two solvent system.[21] After carbonization of ZIF-8 with or without Fe ions (denoted as Fe_{SA}–N–C and N–C, respectively), no characteristic crystalline metal species were identified in the XRD patterns (Fig. S1, ESI†) of the pyrolyzed samples, excluding the formation of large particles. Then, Fe_{SA}–N–C was further used as a substrate for depositing Pt nanoparticles *via* a surfactant-free reduction process to form a $Pt@Fe_{SA}$–N–C composite. The final product ($Pt_A@Fe_{SA}$–N–C) was obtained by annealing treatment of $Pt@Fe_{SA}$–N–C, which results in alloying of Pt and Fe/Zn atoms to form a highly ordered core–shell Pt_3M (M: Fe and Zn) intermetallic structure. This process could also enhance the binding between Pt alloy nanoparticles and the substrate, which prevents the alloy nanoparticles from aggregating under ORR conditions. For comparison, nitrogen doped carbon that anchors Pt alloy ($Pt_A@N–C$) was also prepared by a similar procedure. More experimental details are provided in the ESI.†

In view of the fact that the active sites located within the particles cannot contribute to the ORR activity,[6] and to provide more sites for Pt deposition, we selected a ZIF-8 that is only ~50 nm in diameter as a precursor (Fig. S2, ESI†). This size has also been shown to be the optimal for ZIF-derived catalysts in the literature.[22] After carbonization, the rhombic dodecahedron shape of ZIF-8 was well inherited and no significant particle agglomeration was observed for the N–C sample (Fig. S3, ESI†). For the Fe_{SA}–N–C sample with Fe ions, the particles were slightly agglomerated with the initial rhombic dodecahedron shape somewhat changed (Fig. S4, ESI†), which

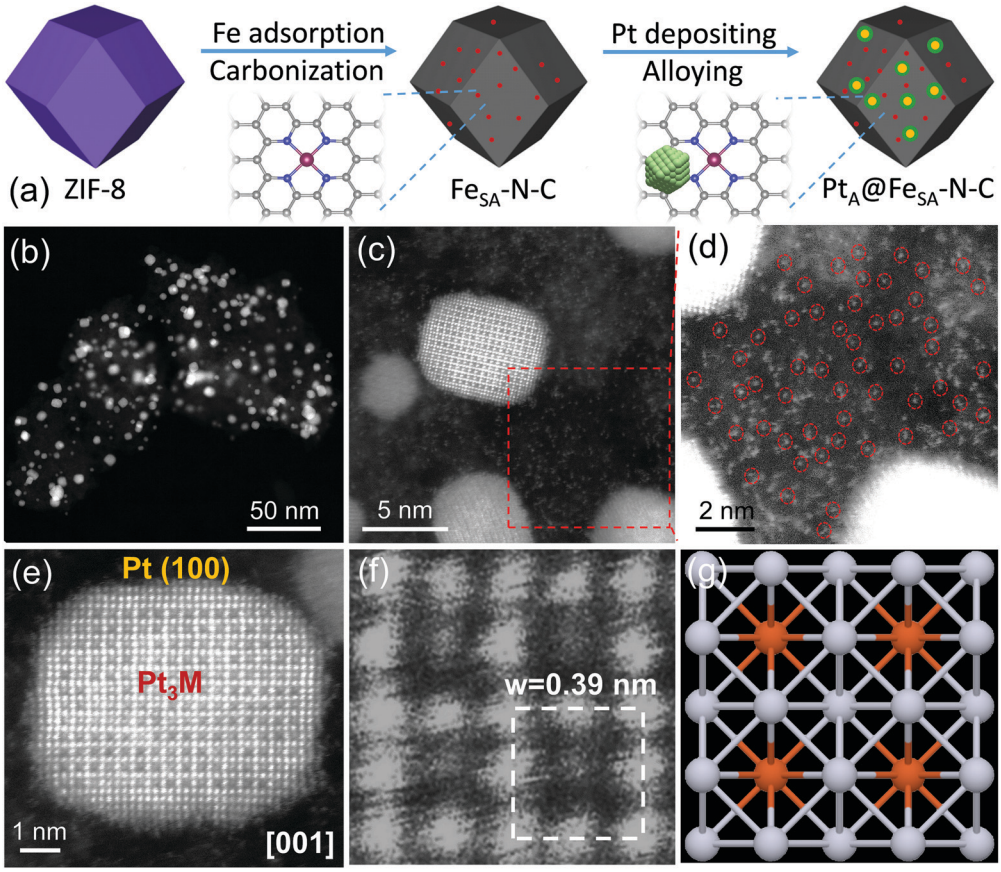

Fig. 1 (a) Schematic illustration of the preparation of $Pt_A@Fe_{SA}$–N–C. (b–e) HAADF-STEM images of $Pt_A@Fe_{SA}$–N–C. (f) A crop of the superlattice feature from (e). (g) Crystal structure of ordered Pt_3M viewed along the [001] zone axis (the red and grey spheres present M and Pt atoms, respectively).

could be ascribed to the accelerated decomposition of metal–imidazolate–metal linkages caused by Fe species. To study the structural information of the Pt alloy and the distribution of Fe in the Fe–N–C substrate of $Pt_A@Fe_{SA}$–N–C, aberration-corrected scanning transmission electron microscopy (AC-STEM) was applied. The high-angle annular dark-field scanning transmission electron microscopy (HAADF-STEM) images demonstrate that the nanoparticles are uniformly and individually distributed on the Fe_{SA}–N–C support (Fig. 1b and Fig. S5, S6, ESI†). The statistical size analysis suggests that the average diameter of these nanoparticles is approximately 4 nm (Fig. S7, ESI†). To investigate the chemical composition and elemental distribution of the nanoparticles, elemental mapping based on energy-dispersive X-ray spectroscopy (EDX) in STEM mode was applied. As shown in Fig. S8 (ESI†), in addition to Pt, the alloy particles also contain Fe and Zn atoms, which are mainly concentrated inside the particle, indicating that the Pt alloy core is surrounded by a Pt shell, and both Fe and Zn atoms participated in the formation of the Pt alloy. The core–shell structure implies the diffusion of transition metal atoms from the Fe–N–C substrate into Pt nanoparticles.[23] The Zn in the alloy may stem from residual Zn after vaporization.[24,25] Since Pt is in excess during the reaction process, a Pt shell forms outside. High-resolution HAADF-STEM measurements were further performed to unravel the detailed structure at the atomic level. Since HAADF-STEM is highly sensitive to the Z-contrast of atoms, Pt atoms have higher intensity than Fe and Zn atoms in the images, while N and C atoms are hard to discern. As shown in Fig. 1c and d and Fig. S9 (ESI†), the Pt alloy nanoparticles are surrounded by densely populated, atomically dispersed Fe and Zn atoms (labelled with red circles in Fig. 1d), which have less imaging contrast than Pt atoms. As Fe-free catalysts (N–C) have been shown to have poor activity that is similar to "metal-free" carbon catalysts, Zn incorporation into the substrate is assumed to play an insignificant role in modifying the ORR activity.[26]

In Fig. 1e, an individual Pt alloy nanoparticle is viewed along the [001] zone axis, exhibiting a core–shell structure composed of an ordered Pt_3M intermetallic core with a Pt-rich shell (3–4 atomic layers). It should be noted that the particle predominately contains Pt(100) crystal facets, with some high-index facets exposed at the corner of the particles (Fig. 1e and Fig. S9, ESI†). It has been found that these high-index facets exhibit higher ORR activity.[12] In the core, the ordered superstructure is clearly indicated by the higher and lower intensity caused by the different Z-contrast of Pt and either Fe or Zn. High magnification (Fig. 1f) further shows that the unit cell consists of a periodic square array of low Z-contrast atom (Fe or Zn) columns surrounded by high Z-contrast atom (Pt) columns at the edges and corners of each unit cell, which is consistent with the crystal structure of Pt_3M (Fig. 1g). Also, the width of the

unit cell is ~0.39 nm, which is equal to the lattice constant of the face-centered cubic Pt_3M lattice.[27,28] The fast Fourier transform (FFT) pattern (Fig. S10, ESI†) further confirms the ordered Pt_3M structure in accordance with previous work.[15] An idealized atomic structure of the Pt_3M core–shell nanoparticle based on the TEM results is schematically shown in Fig. S11 (ESI†).

To further investigate the alloying process and characterize the crystalline phase of the Pt-based nanoparticles, X-ray diffraction (XRD) was employed. The XRD patterns of the samples before ($Pt@Fe_{SA}$–N–C) and after the annealing treatment ($Pt_A@Fe_{SA}$–N–C) are shown in Fig. 2a. Before the heat treatment, there are two broad diffraction peaks centered at ~39.23° and ~24°, which correspond to the (111) plane of Pt metal and the (002) plane of carbon,[29] respectively. Because other diffraction planes of Pt metal were absent, it is likely that the Pt nanoparticles have low crystallinity.[23] After the annealing treatment ($Pt_A@Fe_{SA}$–N–C), the characteristic superlattice peaks of the (100) and (110) planes of ordered Pt_3M were observed (highlighted in grey solid circles), and the peak at around 40° became sharper and stronger, as well as exhibiting an obvious positive shift, and some other peaks whose positions were consistent with the ordered Pt_3M phase emerged, implying the transformation from Pt metal to the ordered Pt_3M alloy. To investigate the surface properties of the catalysts, X-ray photoelectron spectroscopy (XPS) analysis was conducted. Fig. S12 (ESI†) shows the wide scan spectra for the samples and Table S1 (ESI†) summarizes the corresponding elemental composition. It should be noted that some Zn exists in the carbon matrix due to the accumulation of Zn during the evaporation at high temperature, which is a common phenomenon in ZIF-8 derived materials.[20,30–32] The trace amount of Zn in the carbon matrix has a negligible effect on the catalytic activity, evident from the electrochemical performance results to be discussed below. However, the Zn atoms can participate in the formation of ordered Pt_3M alloy to reduce the usage of Pt and improve the durability and activity of the catalysts due to the strain effect and higher utilization of Pt atoms.[13,14,33] As shown in Fig. S12 and Table S1 (ESI†), the N and Fe/Zn content decrease after the formation of the Pt alloy, suggesting that some N–Fe/Zn bonds are broken, and Fe/Zn atoms are alloyed with Pt nanoparticles while N atoms are removed. The decreased doping of the carbon substrate is also supported by Raman results. As shown in Fig. S13 (ESI†), the nature of carbon, as characterized by the intensity ratio of the D band and G band (I_D/I_G), suggested that the samples $Pt_A@Fe_{SA}$–N–C and $Pt_A@N$–C have lower I_D/I_G values (1.01 and 1.07) than Fe_{SA}–N–C and N–C (1.24 and 1.14), which means fewer defects and a higher degree of graphitization.[34] Additionally, the Pt-catalyzed graphitization mechanism during the high-temperature pyrolysis may also contribute to the graphitization of carbon.[35] High-resolution XPS spectra were analyzed to further elucidate the chemical changes after the formation of the ordered Pt-alloy. As shown in Fig. 2b, the N 1s spectra for Fe_{SA}–N–C and $Pt_A@Fe_{SA}$–N–C can be deconvoluted into four peaks associated with pyridinic N (398.4 eV), N–Fe/Zn (399.5 eV), pyrrolic N (400.5 eV) and graphitic N (401.1 eV), respectively.[36] The existence of N–Fe/Zn peaks confirms the coordination between Fe/Zn and N in the carbon support. During the annealing treatment, Fe/Zn atoms are alloyed with Pt nanoparticles and N–Fe/Zn bonds are broken, resulting in a significant decrease of the N content, especially N–Fe/Zn and pyridinic N. For the samples without Fe, the N 1s spectra exhibit the same changes during the annealing

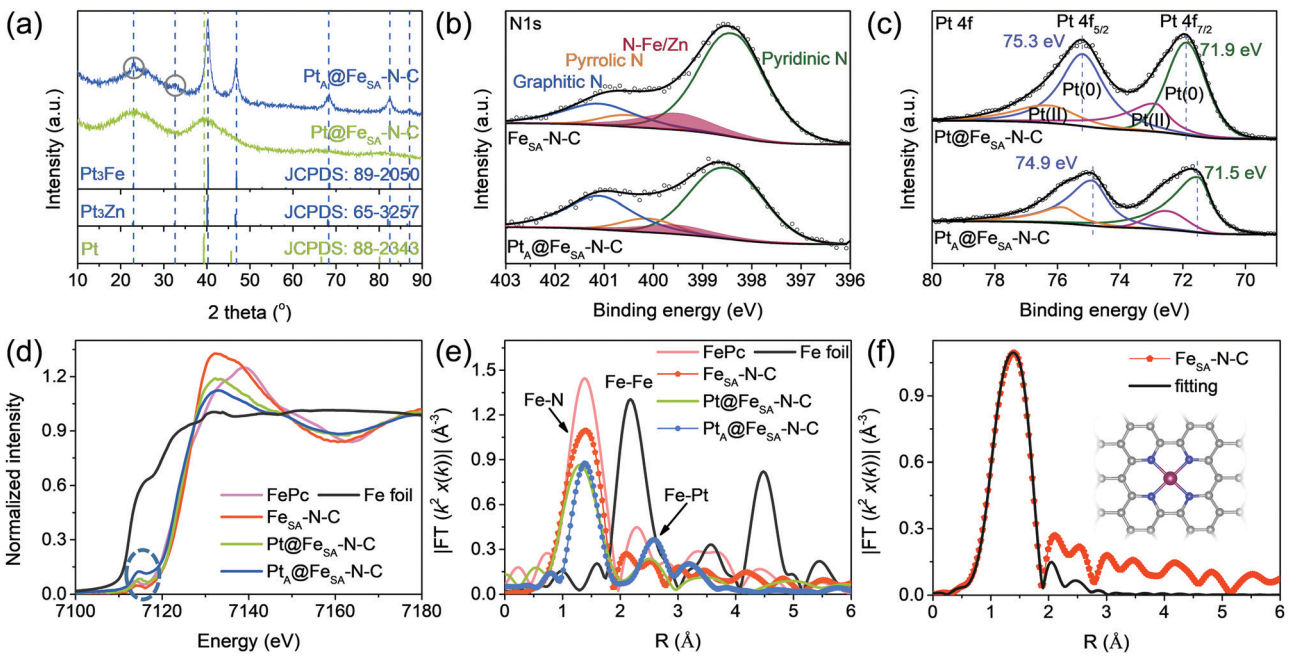

Fig. 2 (a) XRD patterns for $Pt_A@Fe_{SA}$–N–C and $Pt@Fe_{SA}$–N–C. (b) XPS spectra of N 1s for Fe_{SA}–N–C and $Pt_A@Fe_{SA}$–N–C. (c) XPS spectra of Pt 4f for $Pt@Fe_{SA}$–N–C and $Pt_A@Fe_{SA}$–N–C. (d) XANES and (e) FT-EXAFS spectra of Fe_{SA}–N–C, $Pt@Fe_{SA}$–N–C, $Pt_A@Fe_{SA}$–N–C and reference materials at the Fe K-edge. (f) EXAFS fitting for Fe_{SA}–N–C in R-space at the Fe K-edge; the inset shows a model of the isolated Fe environment.

treatment (Fig. S14, ESI†). The high-resolution Pt 4f XPS spectra shown in Fig. 2c indicate that the surfaces of both Pt nanoparticles and Pt-alloy nanoparticles are primarily in the metallic state, while a negative binding energy shift ($\sim$0.4 eV) is observed for the Pt 4f doublet on $Pt_A@Fe_{SA}$–N–C as compared to $Pt@Fe_{SA}$–N–C, indicating the alloying interactions between Pt and Zn/Fe atoms. Theoretically, Pt has higher electronegativity than Zn and Fe, and thus the Pt in the Pt_3M alloy, compared to individual Pt nanoparticles, should be more metallic with a negative shift of the binding energy, which is in good agreement with the XPS results, supporting the formation of the Pt_3M alloy.[37,38]

X-ray absorption fine structure (XAFS) measurements were performed to further analyze the structure at the atomic level. The Fe K-edge X-ray absorption near-edge structure (XANES) spectra of Fe_{SA}–N–C, $Pt@Fe_{SA}$–N–C, and $Pt_A@Fe_{SA}$–N–C with Fe foil and iron phthalocyanie (FePc) as references are shown in Fig. 2d. The valence states of Fe species in all three as-prepared samples are similar to Fe^{2+} in FePc, since the absorption edges of them are located in a similar place.[39] Among them, the absorption edge of $Pt_A@Fe_{SA}$–N–C showed a slight shift toward lower energy compared to Fe_{SA}–N–C and $Pt@Fe_{SA}$–N–C, indicating that some Fe^{2+} in the carbon matrix was reduced during the alloying process. In the pre-edge region, the fingerprint peak at $\sim$7114 eV was seen in the spectra of all the samples with the Fe_{SA}–N–C substrate (highlighted by the dash circle), providing evidence for the existence of the square-planar Fe–N_4 configuration with a porphyrin-like structure, which is different from the case of Fe foil but the same as the case of FePc.[6,29,40,41] Since our samples were prepared by pyrolysis at 900 °C in argon in the presence of ZIF-derived carbon, the pre-edge peaks at $\sim$7114 eV in the XANES spectra correspond to Fe–N_4, not Fe_2O_3,[42] because the presence of Fe_2O_3 is unlikely (any iron oxide would be reduced to metallic iron by the carbon). In addition, the Fe–N_4 coordination structure was further confirmed by the EXAFS results to be discussed below. The Fourier transform (FT) EXAFS spectra of the corresponding samples and references are shown in Fig. 2e. The spectra of all three Fe_{SA}–N–C-based samples present a primary peak located at $\sim$1.5 Å, which is attributed to the scattering of Fe–N. Moreover, no obvious Fe–Fe peak at $\sim$2.2 Å was detected, confirming that the Fe atoms are stabilized by N atoms and are atomically dispersed. It is worth noting that although some Fe atoms should exist in the Pt_3M alloy in $Pt_A@Fe_{SA}$–N–C, the distance between M atoms in Pt_3M is much longer than 2.2 Å (Fig. 1g) and the content of Fe in Pt_3M is low. Compared with Fe_{SA}–N–C and $Pt@Fe_{SA}$–N–C, an additional peak at $\sim$2.6 Å was presented, corresponding to the Fe–Pt scattering path, further confirming the formation of the Pt_3M alloy.[43,44] EXAFS fitting for Fe_{SA}–N–C was carried out to quantify the chemical environment of typical Fe single atoms in the catalysts. The fitting curve is given in Fig. 2f with fitting parameters listed in Table S2 (ESI†). The fitting result shows that one Fe atom is coordinated with four N atoms at $\sim$1.98 Å, forming an Fe–N_4 moiety (Fig. 2f, inset). To evaluate the porosity of $Pt_A@Fe_{SA}$–N–C, we performed nitrogen adsorption–desorption isotherm measurement (Fig. S15, ESI†). The high specific surface area of 331 $m^2\ g^{-1}$ with a highly porous structure of the catalyst may facilitate mass transfer in electrochemical reactions.

To evaluate the ORR performance of $Pt_A@Fe_{SA}$–N–C and the possible interaction between Pt-alloy nanoparticles and the atomically dispersed Fe sites, electrochemical measurements of various catalysts were first carried out for comparison using a rotating disk electrode (RDE) in a three-electrode cell with a 0.1 M $HClO_4$ electrolyte at room temperature. As shown in Fig. 3a, the ORR activities were measured by linear sweep voltammetry (LSV) in O_2-saturated electrolyte at a rotation speed of 1600 rpm. Obviously, $Pt_A@Fe_{SA}$–N–C catalyst with multiple active sites exhibited the highest activity. $Pt_A@N$–C showed lower activity than the commercial Pt/C (HiSPEC 3000), while the Fe_{SA}–N–C sample without Pt species had relatively poor activity in acidic media, consistent with previous work.[31,45] The N–C sample has little catalytic activity, similar to some of the metal-free carbon catalysts reported previously,[26,46] suggesting that the residual Zn species in the N–C substrate play an insignificant role in the ORR activity, which is consistent with a previous report.[30] Fig. 3b shows the corresponding Tafel plots of various catalysts, where J_k is the kinetic current density calculated from the Koutecky–Levich (K–L) equation.[47] $Pt_A@Fe_{SA}$–N–C shows a small Tafel slope of 64 mV dec^{-1} (where dec means decade), comparable to that of Pt/C (63 mV dec^{-1}) and lower than those of $Pt_A@N$–C (84 mV dec^{-1}) and Fe_{SA}–N–C (66 mV dec^{-1}), indicating fast kinetics towards the ORR. The corresponding $E_{1/2}$ of each catalyst is summarized in Fig. 3c. $Pt_A@Fe_{SA}$–N–C exhibited the highest activity with an $E_{1/2}$ of 0.923 V, which is 92 mV higher than that of $Pt_A@N$–C, 184 mV higher than that of Fe_{SA}–N–C, even better than that of the commercial Pt/C ($E_{1/2}$ = 0.892 V), and superior or comparable to those of very recently reported Pt-based catalysts (Table S3, ESI†). Sample N–C without Fe and Pt species has almost no activity for the ORR in acidic electrolyte, indicating the significant role of the single-atom Fe active sites and Pt_3M alloy for the ORR. Besides the extra active sites in the sample $Pt_A@Fe_{SA}$–N–C, another important reason for the enhanced ORR catalytic activity should be the interaction between Fe_{SA}–N–C and the Pt alloy, implied by the fact that the J_k value of $Pt_A@Fe_{SA}$–N–C is much larger than the sum of those of $Pt_A@N$–C and Fe_{SA}–N–C (Fig. S16, ESI†).[48]

Fig. S17 (ESI†) shows the cyclic voltammetry (CV) curves of $Pt_A@Fe_{SA}$–N–C and Pt/C recorded in N_2-saturated 0.1 M $HClO_4$ solution at a scan rate of 200 mV s^{-1}. The electrochemically active surface area (ECSA) was measured by the hydrogen underpotential deposition (Hupd) method, which assumes a charge density of 210 μC cm^{-2} for one monolayer of hydrogen desorption on Pt. The Pt content of sample $Pt_A@Fe_{SA}$–N–C (13.1 wt%) was determined by inductively coupled plasma optical emission spectrometry (ICP-OES), which is lower than that of 20% Pt/C. The ECSA of $Pt_A@Fe_{SA}$–N–C was estimated to be 65.02 $m^2\ g_{Pt}^{-1}$, slightly larger than that of commercial Pt/C (56.81 $m^2\ g_{Pt}^{-1}$). To provide a comparison of the intrinsic ORR activity, the mass and specific activities were evaluated through normalizing J_k at 0.9 V and 0.85 V by the corresponding mass and ECSA of Pt. As shown in Fig. S18 (ESI†), the mass and

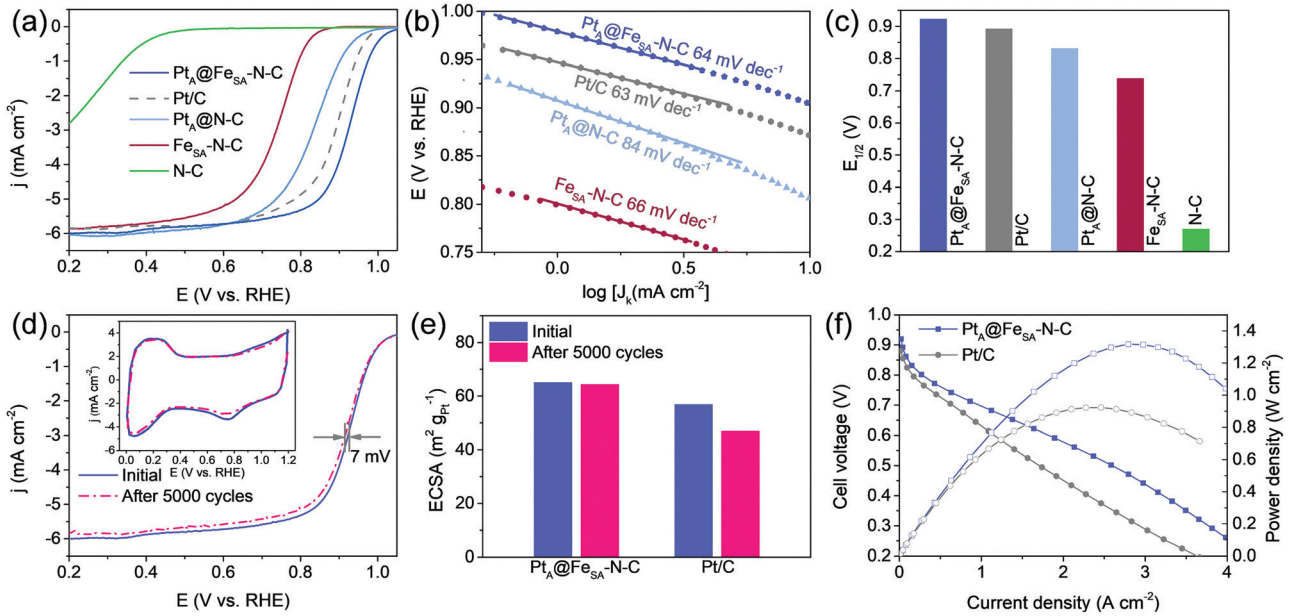

Fig. 3 (a) LSV curves of different catalysts recorded at a scan rate of 10 mV s^{-1} and a rotation rate of 1600 rpm in O_2-saturated 0.1 M $HClO_4$. (b) Tafel plots of the corresponding LSV curves. (c) $E_{1/2}$ of various catalysts in 0.1 M $HClO_4$. (d) LSV curves of $Pt_A@Fe_{SA}$–N–C before and after the durability test. The inset shows the CV curves at a scan rate of 200 mV s^{-1} before and after the durability test. (e) Evaluations of calculated ECSAs for $Pt_A@Fe_{SA}$–N–C and Pt/C before and after the durability tests. (f) The *I*–*V* (solid symbols and lines) and *I*–*P* (hollow symbols and dashed lines) curves of the H_2–O_2 fuel cell. The cathode loading is 0.13 mg_{Pt} cm^{-2}; the pressure is 1.0 bar; and the cell temperature is 65 °C.

specific activities of $Pt_A@Fe_{SA}$–N–C were significantly higher than those of commercial Pt/C. The durability of $Pt_A@Fe_{SA}$–N–C and Pt/C was examined with an ADT by cycling in the potential range of 0.6–1.0 V at a scan rate of 50 mV s^{-1}. In this potential range, the performance degradation was widely believed to be due to crystallite dissolution and agglomeration.[5] Fig. 3d shows the ORR polarization curves of $Pt_A@Fe_{SA}$–N–C before and after the durability test. After 5000 cycles, $E_{1/2}$ decreased by only 7 mV. The inset of Fig. 3d shows that there is no significant change of the CV curves during the ADT. Compared with $Pt_A@Fe_{SA}$–N–C, the degradation of commercial Pt/C (Fig. S19, ESI†) was relatively severe with a 22 mV negative shift of $E_{1/2}$ in the ORR polarization curve after 5000 cycles. To explore the effect of the Fe in the ZIF-derived carbon on the durability of the as-prepared composite catalyst, we performed an ADT for the Pt_A@N–C sample with Pt-alloy but without Fe in the composite. As shown in Fig. S20 (ESI†), $E_{1/2}$ of Pt_A@N–C decreased significantly (by 29 mV) after 5000 CV cycles, indicating that the presence of Fe in the ZIF-derived carbon can improve the stability. CV curves were also obtained before and after ADT to evaluate the change in the ECSA during the ADT. As shown in Fig. 3e, the ECSA of $Pt_A@Fe_{SA}$–N–C almost remained the same after 5000 cycles, while only 83% ECSA was maintained for commercial Pt/C after 5000 cycles. The enhanced ORR durability is likely due to the stable ordered Pt_3M structure in the core and the interaction of the Pt alloy with Fe–N_4 sites, which enhances the binding, helping to prevent the segregation of the Pt alloy and substrate.[10,20] Additionally, the alloying process between Pt and Zn/Fe atoms in the substrate allow the formed Pt-alloy nanoparticles to firmly adhere to the Fe–N–C substrate.

Moreover, the PEMFC performance was evaluated by incorporating the $Pt_A@Fe_{SA}$–N–C catalyst in the cathode of membrane electrode assemblies (MEAs) through a spray deposition method with a cathode Pt loading of 0.13 mg_{Pt} cm^{-2}, where the anode Pt loading was 0.2 mg_{Pt} cm^{-2}. An MEA with a commercial Pt/C cathode with the same Pt loading was also prepared for comparison. Fig. 3f shows the current–voltage (*I*–*V*) curves and current–power (*I*–*P*) characteristics measured under 1.0 bar of humidified H_2–O_2. As expected, the MEA with $Pt_A@Fe_{SA}$–N–C as the cathode catalyst delivered a higher electrochemical performance with a maximum power density of 1.31 W cm^{-2} at 2.81 A cm^{-2} compared to the MEA using commercial Pt/C as the cathode catalyst (0.92 W cm^{-2} at 2.46 A cm^{-2}). Moreover, $Pt_A@Fe_{SA}$–N–C demonstrated a high mass activity of 0.45 A mg_{Pt}^{-1} in the MEA test at a voltage of 0.9 V, exceeding the U.S. Department of Energy (DOE) target of 0.44 A mg_{Pt}^{-1}. Due to the porous nature of ZIF-derived carbon, which increases the thickness of the electrode layer, the fuel cell using $Pt_A@Fe_{SA}$–N–C shows a relatively faster voltage loss at a high current density range. However, the porous structure of the ZIF-derived carbon support can enhance the mass transport to some extent, allowing the active sites to participate in the ORR even in the high current region.[6] Furthermore, the durability of the MEAs was also evaluated with an ADT using CV from 0.6 to 0.95 V according to DOE catalyst stability evaluation protocols. Fuel cell polarizations were periodically measured after designated voltage cycles up to 10 000. As shown in Fig. S21 (ESI†), compared with the MEA with a Pt/C cathode catalyst, the MEA with a $Pt_A@Fe_{SA}$–N–C cathode catalyst demonstrated enhanced durability with its mass activity retained at 9.54 A mg_{Pt}^{-1} at 0.6 V after 10 000 potential cycles, reaching 75.6% of the initial value.

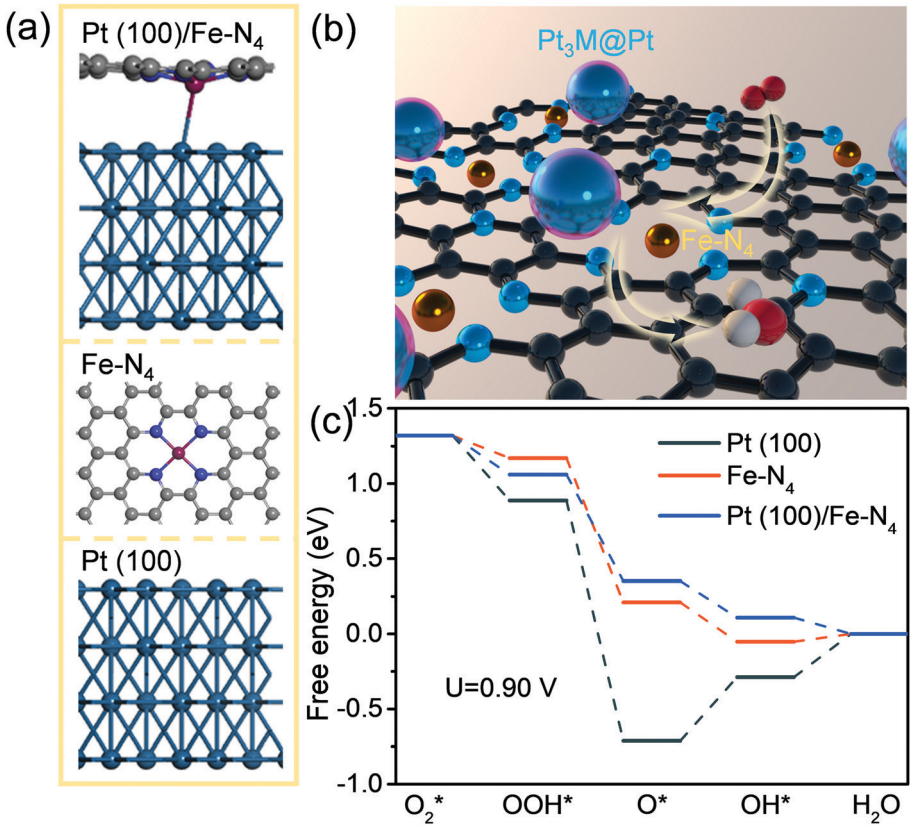

Fig. 4 (a) Computational models of Pt(100)/Fe–N_4, Fe–N_4 and Pt(100). (b) Schematic of Pt_A@Fe_{SA}–N–C. The big core–shell spheres represent Pt-alloy nanoparticles; gold, blue, black, red and white spheres represent Fe, N, C, O and H atoms, respectively. (c) Free-energy path of the ORR at U = 0.9 V for the three models constructed.

On the basis of electrochemical analysis by RDE, there should be an interaction between the Pt alloy and single-atom Fe active sites. To further elaborate it, we performed density functional theory (DFT) calculations to investigate the ORR activities of Pt_A@Fe_{SA}–N–C catalyst systems with the computational hydrogen electrode (CHE) model. Pt(100) was chosen to represent the Pt alloy nanoparticle because its surface is covered with a 3–4 atomic-layer-thick Pt shell (Fig. 1e). As shown in Fig. 4a, three models including Pt(100)/Fe–N_4, Pt(100), and Fe–N_4 were constructed according to the characteristics of the Pt_A@Fe_{SA}–N–C catalyst, schematically depicted in Fig. 4b. In the Pt(100)/Fe–N_4 model, the interlayer spacing between Pt(100) and FeN_4 is 2.74 Å, determined through energy optimization. Fig. S22 (ESI†) shows the atomic structures of the adsorption configurations and Table S4 (ESI†) shows the adsorption Gibbs free energies (eV) of the reaction intermediate O* (ΔG_O), OH* (ΔG_{OH}), and OOH* (ΔG_{OOH}), which were calculated based on the reversible hydrogen electrode (RHE) model proposed by Nørskov *et al.*[49] For an ideal $4e^-$ ORR electrocatalyst, the reaction free energies of every step would be 1.23 eV at zero potential. Here, the onset potential is used to measure the ORR performance, referring to the absolute value of the potential determining step in the four reaction free energies. The free energy diagram for the ORR is shown in Fig. 4c and Fig. S23 (ESI†), and the corresponding values can be found in Tables S5 and S6 (ESI†). The data indicate that the rate-determining step for Pt(100)/Fe–N_4 and Fe–N_4 is the desorption of the OH* intermediate as water, while the rate-determining step for Pt(100) is the step from O* to OH*. For the Pt(100)/Fe–N_4 model, the computed onset potential is 1.01 V, which is higher than those of Pt(100) (0.48 V) and Fe–N_4 (0.85 V), indicating that the interaction between Pt(100) and Fe–N_4 can improve the catalytic activity of Fe sites for the ORR. This is mainly because the Pt atom is more electronegative than the Fe atom. The origin of the catalytic activity arose from the observed charge transfer from the Fe atom to the Pt atom, leading to a more positive charge on the Fe atom, resulting in a weaker adsorption strength of the OH* intermediate (Table S4, ESI†). Theoretical calculations suggest that the ORR activity of the Fe–N_4 sites may be enhanced by adjacent Pt(100).

Thus, the high activity of the as-developed composite catalyst could be mainly attributed to the ordered intermetallic Pt-alloy nanoparticles as demonstrated by the experimental results and the favorable Fe–N_4 active sites affected by Pt as unraveled by the theoretical calculations.

Conclusions

In summary, we designed and successfully synthesized a highly active ORR electrocatalyst composed of core–shell Pt alloy

nanoparticles on an Fe–N–C substrate with atomically dispersed single Fe atoms, which demonstrates significantly enhanced activity and durability in both RDE measurements and fuel cell tests. The enhanced performance is attributed not only to the unique structure of the catalyst such as the Pt shell and the stable ordered intermetallic Pt_3M core, as revealed and qualified using AC-STEM, XAFS and other techniques, but also to an interaction between the Pt alloy nanoparticles and the single-atom Fe active sites. This study confirmed an effective strategy for designing promising ORR electrocatalysts by combining a non-precious single-atom catalyst with a core–shell Pt alloy nanoparticle catalyst, which enhances the catalytic activity and durability while reducing the usage of Pt.

Conflicts of interest

There are no conflicts to declare.

Acknowledgements

This work was supported by the US National Science Foundation under award number DMR-1742828, and the National Natural Science Foundation of China (Grants No. 51972129). X. A. acknowledges the financial support of a scholarship from the China Scholarship Council (CSC).

References

1 H. A. Gasteiger and N. M. Marković, *Science*, 2009, **324**, 48–49.
2 M. K. Debe, *Nature*, 2012, **486**, 43.
3 Y.-J. Wang, N. Zhao, B. Fang, H. Li, X. T. Bi and H. Wang, *Chem. Rev.*, 2015, **115**, 3433–3467.
4 Y. Xiong, Y. Yang, F. J. DiSalvo and H. C. D. Abruña, *J. Am. Chem. Soc.*, 2018, **140**, 7248–7255.
5 R. Borup, J. Meyers, B. Pivovar, Y. S. Kim, R. Mukundan, N. Garland, D. Myers, M. Wilson, F. Garzon and D. Wood, *Chem. Rev.*, 2007, **107**, 3904–3951.
6 X. Wan, X. Liu, Y. Li, R. Yu, L. Zheng, W. Yan, H. Wang, M. Xu and J. Shui, *Nat. Catal.*, 2019, **2**, 259.
7 X. Ao, W. Zhang, Z. Li, J.-G. Li, L. Soule, X. Huang, W.-H. Chiang, H. M. Chen, C. Wang, M. Liu and X. C. Zeng, *ACS Nano*, 2019, **13**, 11853–11862.
8 W. Tu, K. Chen, L. Zhu, H. Zai, B. E. X. Ke, C. Chen, M. Sui, Q. Chen and Y. Li, *Adv. Funct. Mater.*, 2019, **29**, 1807070.
9 D. Banham and S. Ye, *ACS Energy Lett.*, 2017, **2**, 629–638.
10 X. X. Wang, S. Hwang, Y.-T. Pan, K. Chen, Y. He, S. Karakalos, H. Zhang, J. S. Spendelow, D. Su and G. Wu, *Nano Lett.*, 2018, **18**, 4163–4171.
11 C. Chen, Y. Kang, Z. Huo, Z. Zhu, W. Huang, H. L. Xin, J. D. Snyder, D. Li, J. A. Herron and M. Mavrikakis, *Science*, 2014, **343**, 1339–1343.
12 M. Luo, Y. Sun, X. Zhang, Y. Qin, M. Li, Y. Li, C. Li, Y. Yang, L. Wang and P. Gao, *Adv. Mater.*, 2018, **30**, 1705515.
13 J. Li, Z. Xi, Y.-T. Pan, J. S. Spendelow, P. N. Duchesne, D. Su, Q. Li, C. Yu, Z. Yin and B. Shen, *J. Am. Chem. Soc.*, 2018, **140**, 2926–2932.
14 Q. Li, L. Wu, G. Wu, D. Su, H. Lv, S. Zhang, W. Zhu, A. Casimir, H. Zhu and A. Mendoza-Garcia, *Nano Lett.*, 2015, **15**, 2468–2473.
15 D. Wang, H. L. Xin, R. Hovden, H. Wang, Y. Yu, D. A. Muller, F. J. DiSalvo and H. D. Abruña, *Nat. Mater.*, 2013, **12**, 81.
16 S. Sui, X. Wang, X. Zhou, Y. Su, S. Riffat and C.-J. Liu, *J. Mater. Chem. A*, 2017, **5**, 1808–1825.
17 J. Salgado, F. Alcaide, G. Álvarez, L. Calvillo, M. Lázaro and E. Pastor, *J. Power Sources*, 2010, **195**, 4022–4029.
18 S. H. Joo, H. I. Lee, D. J. You, K. Kwon, J. H. Kim, Y. S. Choi, M. Kang, J. M. Kim, C. Pak and H. Chang, *Carbon*, 2008, **46**, 2034–2045.
19 X. Ao, W. Zhang, Z. Li, L. Lv, Y. Ruan, H.-H. Wu, W.-H. Chiang, C. Wang, M. Liu and X. C. Zeng, *J. Mater. Chem. A*, 2019, **7**, 11792–11801.
20 L. Chong, J. Wen, J. Kubal, F. G. Sen, J. Zou, J. Greeley, M. Chan, H. Barkholtz, W. Ding and D.-J. Liu, *Science*, 2018, **362**, 1276–1281.
21 A. Aijaz, A. Karkamkar, Y. J. Choi, N. Tsumori, E. Rönnebro, T. Autrey, H. Shioyama and Q. Xu, *J. Am. Chem. Soc.*, 2012, **134**, 13926–13929.
22 H. Zhang, S. Hwang, M. Wang, Z. Feng, S. Karakalos, L. Luo, Z. Qiao, X. Xie, C. Wang and D. Su, *J. Am. Chem. Soc.*, 2017, **139**, 14143–14149.
23 J. Li, G. Wang, J. Wang, S. Miao, M. Wei, F. Yang, L. Yu and X. Bao, *Nano Res.*, 2014, **7**, 1519–1527.
24 Z. Wang, H. Jin, T. Meng, K. Liao, W. Meng, J. Yang, D. He, Y. Xiong and S. Mu, *Adv. Funct. Mater.*, 2018, **28**, 1802596.
25 Q. Ren, H. Wang, X. F. Lu, Y. X. Tong and G. R. Li, *Adv. Sci.*, 2018, **5**, 1700515.
26 G. Wu, K. L. More, C. M. Johnston and P. Zelenay, *Science*, 2011, **332**, 443–447.
27 L. J. Cabri and C. E. Feather, *Can. Mineral.*, 1975, **13**, 117–126.
28 H. Nowotny, E. Bauer, A. Stempfl and H. Bittner, *Monatsh. Chem.*, 1952, **83**, 221–236.
29 Y. Chen, Z. Li, Y. Zhu, D. Sun, X. Liu, L. Xu and Y. Tang, *Adv. Mater.*, 2019, **31**, 1806312.
30 X. X. Wang, D. A. Cullen, Y. T. Pan, S. Hwang, M. Wang, Z. Feng, J. Wang, M. H. Engelhard, H. Zhang and Y. He, *Adv. Mater.*, 2018, **30**, 1706758.
31 M. Xiao, J. Zhu, L. Ma, Z. Jin, J. Ge, X. Deng, Y. Hou, Q. He, J. Li and Q. Jia, *ACS Catal.*, 2018, **8**, 2824–2832.
32 H. Zhang, H. T. Chung, D. A. Cullen, S. Wagner, U. I. Kramm, K. L. More, P. Zelenay and G. Wu, *Energy Environ. Sci.*, 2019, **12**, 2548–2558.
33 W. Wang, B. Lei and S. Guo, *Adv. Energy Mater.*, 2016, **6**, 1600236.
34 X. Ao, H. Sun, C. Wang, J. Li, Y. Ruan, B. Li, Q.-H. Wu, Y. Li, J. Jiang and Y. Yang, *Carbon*, 2018, **130**, 599–606.
35 R. Lamber and N. I. Jaeger, *Surf. Sci.*, 1993, **289**, 247–254.
36 Z. Lu, B. Wang, Y. Hu, W. Liu, Y. Zhao, R. Yang, Z. Li, J. Luo, B. Chi and Z. Jiang, *Angew. Chem.*, 2019, **131**, 2648–2652.

37 J. Alonso and L. Girifalco, *Phys. Rev. B: Condens. Matter Mater. Phys.*, 1979, **19**, 3889.
38 X. Tian, X. Zhao, Y.-Q. Su, L. Wang, H. Wang, D. Dang, B. Chi, H. Liu, E. J. Hensen and X. W. D. Lou, *Science*, 2019, **366**, 850–856.
39 Q. Li, W. Chen, H. Xiao, Y. Gong, Z. Li, L. Zheng, X. Zheng, W. Yan, W. C. Cheong and R. Shen, *Adv. Mater.*, 2018, **30**, 1800588.
40 Y. Deng, B. Chi, J. Li, G. Wang, L. Zheng, X. Shi, Z. Cui, L. Du, S. Liao and K. Zang, *Adv. Energy Mater.*, 2019, **9**, 1802856.
41 Q. Liu, X. Liu, L. Zheng and J. Shui, *Angew. Chem. Int. Ed.*, 2018, **57**, 1204–1208.
42 F. Xiao, G.-L. Xu, C.-J. Sun, M. Xu, W. Wen, Q. Wang, M. Gu, S. Zhu, Y. Li and Z. Wei, *Nano Energy*, 2019, **61**, 60–68.
43 W. Chen, W. Gao, P. Tu, T. Robert, Y. Ma, H. Shan, X. Gu, W. Shang, P. Tao and C. Song, *Nano Lett.*, 2018, **18**, 5905–5912.
44 M. Jiang, W. Liu, X. Yang, Z. Jiang, T. Yao, S. Wei and X. Peng, *ACS Nano*, 2015, **9**, 10950–10960.
45 L. Yang, D. Cheng, H. Xu, X. Zeng, X. Wan, J. Shui, Z. Xiang and D. Cao, *Proc. Natl. Acad. Sci. U. S. A.*, 2018, **115**, 6626–6631.
46 Z. Yang, Y. Wang, M. Zhu, Z. Li, W. Chen, W. Wei, T. Yuan, Y. Qu, Q. Xu and C. Zhao, *ACS Catal.*, 2019, **9**, 2158–2163.
47 X. Ao, X. Xue, Z. Yang, Y. Yang and C. Wang, *Mater. Today Energy*, 2019, **12**, 62–69.
48 H. Shen, E. Gracia-Espino, J. Ma, K. Zang, J. Luo, L. Wang, S. Gao, X. Mamat, G. Hu and T. Wagberg, *Angew. Chem., Int. Ed.*, 2017, **56**, 13800–13804.
49 J. K. Nørskov, J. Rossmeisl, A. Logadottir, L. Lindqvist, J. R. Kitchin, T. Bligaard and H. Jónsson, *J. Phys. Chem. B*, 2004, **108**, 17886–17892.

